Developing improved Lagrangian point particle models of gas-solid flow from particle-resolved direct numerical simulation

By S. Subramaniam†, M. Mehrabadi†, J. Horwitz AND A. Mani

Lagrangian point-particle models are widely used to model particle-laden flows in Reynolds Average Navier-Stokes (RANS) simulation, Large Eddy Simulation (LES) and Direct Numerical Simulation (DNS) codes. Point-particle models do not impose the exact boundary conditions corresponding to particle-fluid interaction, but rather they employ a particle acceleration model to represent the fluid-particle interaction. In two-way coupled problems the effect of the solid particles on fluid phase momentum balance is accomplished through an interphase coupling algorithm. Both the drag law and the interphase coupling algorithm affect the accuracy with which the coupled mean momentum and kinetic energy equations are solved. In this study we use particle-resolved direct numerical simulation (PR-DNS) in decaying isotropic turbulent flow to assess the accuracy of point-particle acceleration models, and also their implication for interphase energy transfer in point-particle direct numerical simulation (PP-DNS). Our results indicate that a steady drag model for particle acceleration underpredicts the true particle acceleration. In addition, the particle kinetic energy and viscous dissipation are also underpredicted. These discrepancies are traced to the simple form of the particle acceleration model, and motivate improvements.

1. Introduction

Interaction of solid particles with a turbulent flow is very common in nature and in industrial applications. Natural events include transport of volcanic ash in the atmosphere as well as sedimentation of solid particles in rivers. The industrial application that motivates this study is a solar receiver in which particles absorb solar energy by radiation, generating buoyant flow motions that lead to generation of a turbulent flow (Zamansky *et al.* 2014). Understanding particle-turbulence interaction is essential for better predictive modeling of particle-laden flows in natural events and of industrial applications.

Particle-laden flow problems are characterized by high-dimensional parameter space including particle-to-fluid density ratio $\rho^{(p)}/\rho^{(f)}$, mass loading, particle Stokes number $\mathrm{St}_\eta = \tau_p/\tau_\eta$ with $\tau_p = \rho^{(p)} d_p^2/18\rho^{(f)}\nu^{(f)}$ and τ_η being, respectively, the particle response time and Kolmogorov time scale, particle Reynolds number $\mathrm{Re}_p = u' d_p/\nu^{(f)}$ with u' being a fluid-phase velocity scale, and particle diameter to Kolmogorov length scale ratio d_p/η. The choice of numerical method depends on the region of the parameter space that is accessed by the particle-laden flow.

If particles are much smaller than the Kolmogorov length scale ($d_p < \eta$), the point-particle assumption is valid in the Lagrangian-Eulerian (LE) representation of particle-laden flow (Balachandar & Eaton 2010), where particles are described in a Lagrangian

† Department of Mechanical Engineering, Iowa State University

frame and the carrier flow is described in an Euleriran frame. The effect of fluid-particle interaction in the form of the hydrodynamic force on a particle can be represented by a drag model. The Maxey-Riley-Gatognol equation provides a complete description of particle acceleration that accounts for contributions from various fluid-solid interaction mechanisms (Crowe *et al.* 2011). These contributions are from the (a) undisturbed carrier flow, (b) steady state drag, (c) virtual mass, (d) history term, (e) Saffman lift, and (f) Magnus lift. Depending on the regime of gas-solid flow, some of these contributions may or may not be important. For instance, when particle-to-fluid density ratio is high, the virtual mass force becomes negligible. Therefore, different terms in the Maxey-Riley-Gatognol equation may be significant depending on $\rho^{(p)}/\rho^{(f)}$ and flow time scales for particle acceleration model in LE simulations of gas-solid flows, although for simplicity the steady drag model is used in many applications.

In the current study we are interested in investigating the accuracy of using the steady drag model in predicting true particle acceleration in a turbulent particle-laden flow. It is also of interest to examine the implication of modeled particle acceleration on the kinetic energy of fluctuating velocities in the fluid phase $k^{(f)}$ and the solid phase $k^{(p)}$ as well as the viscous dissipation $\varepsilon^{(f)}$. For this assessment, we perform PR-DNS of turbulent particle-laden flow in a regime where the PP-DNS approach is valid and then compare the evolution of $k^{(f)}$, $k^{(p)}$ and $\varepsilon^{(f)}$ between the two approaches. Thus, we can isolate the effect of the particle acceleration model on the evolution of the aforementioned quantities. To the best of the our knowledge, this study involving the direct comparison between PR-DNS and PP-DNS is the first of its kind because the resolution requirement of PR-DNS makes it prohibitively expensive to simulate in a parameter regime also applicable to PP-DNS.

The rest of this report reads as follows. In Section 2, the kinetic energy equations of the gas-phase and the solid-phase and also the conservation of interphase TKE transfer principle are presented. In Section 3 PR-DNS and PP-DNS methods are described. In Section 4 simulation results are presented which are followed by discussions in Section 5. Finally, we summarize our findings and discuss future outlook for this work in Section 6.

2. Kinetic energy of fluctuating velocities

The evolution equation of gas-phase kinetic energy for a homogeneous gas-solid suspension is given by

$$\rho^{(f)}(1-\phi)\frac{dk^{(f)}}{dt} = \Pi^{(f)} - \varepsilon^{(f)} \tag{2.1}$$

(Xu & Subramaniam 2007; Pai & Subramaniam 2009), where $\rho^{(f)}$ is the gas-phase density, ϕ is the solid-phase volume fraction, $\Pi^{(f)}$ is the fluid-phase interphase turbulent kinetic energy (TKE) transfer, and $\varepsilon^{(f)}$ is the viscous dissipation. The evolution equation for the solid-phase kinetic energy $k^{(p)}$ in a homogeneous system is

$$\rho^{(p)}\phi\frac{dk^{(p)}}{dt} = \Pi^{(p)}, \tag{2.2}$$

where $\Pi^{(p)}$ is the solid-phase interphase TKE transfer. Note that in the above expression particle collisions are assumed to be elastic. Therefore, there is no energy loss owing to particle-particle interaction in the form of particle collisions. The mixture kinetic energy $e^{(m)}$ is defined as $\rho^{(f)}(1-\phi)k^{(f)} + \rho^{(p)}\phi\, k^{(p)}$ which is the mass-weighted kinetic energy in the system. We can derive an evolution equation for the mixture energy by simply

adding Eqs. (2.1) and (2.2). The principle of conservation of interphase TKE transfer first proposed by Xu & Subramaniam (2007) states that for a gas-solid system with zero mean slip velocity, the gas-phase and solid-phase interphase TKE transfer terms are conservative, i.e., $\Pi^{(f)}+\Pi^{(p)}=0$. Applying this principle to the mixture energy equation reveals that

$$\frac{de^{(m)}}{dt}=\Pi^{(f)}+\Pi^{(p)}-\varepsilon^{(f)}=-\varepsilon^{(f)}. \tag{2.3}$$

Therefore, the mixture energy monotonically decays by only the viscous dissipation in the absence of any driving force.

In the PP-DNS approach, the evolution equations of $k^{(f)}$, $k^{(p)}$ and $e^{(m)}$ for a homogeneous gas-solid system with elastic particle collisions are given as

$$\begin{aligned}\rho^{(f)}(1-\phi)\frac{dk^{(f)}}{dt}&=\Pi^{(f)}_{pp}-\varepsilon^{(f)}_{pp},\\ \rho^{(p)}\phi\frac{dk^{(p)}}{dt}&=\Pi^{(p)}_{pp},\\ \frac{de^{(m)}}{dt}&=\Pi^{(f)}_{pp}+\Pi^{(p)}_{pp}-\varepsilon^{(f)}_{pp}.\end{aligned} \tag{2.4}$$

In the above equations, the subscript *pp* denotes point-particle approach quantities. Sundaram & Collins (1996) showed that if particle acceleration is modeled by a linear steady drag model of the form

$$\frac{d\mathbf{u}^{(p)}}{dt}=\frac{\mathbf{u}^{(f)}_{\mathbf{x}_p}-\mathbf{u}^{(p)}}{\tau_p}, \tag{2.5}$$

with $\mathbf{u}^{(f)}_{\mathbf{x}_p}$ and $\mathbf{u}^{(p)}$ being, respectively, the fluid-phase velocity at the particle location and the particle velocity, then the summation of fluid-phase and solid-phase interphase TKE transfers is

$$\Pi^{(f)}_{pp}+\Pi^{(p)}_{pp}=-\rho^{(p)}\phi\left\langle\frac{(\mathbf{u}^{(f)}_{\mathbf{x}_p}-\mathbf{u}^{(p)})\cdot(\mathbf{u}^{(f)}_{\mathbf{x}_p}-\mathbf{u}^{(p)})}{\tau_p}\right\rangle=-\varepsilon^{*}_{pp}, \tag{2.6}$$

which is non-zero and violates the conservation principle of interphase TKE transfer (Xu & Subramaniam 2007). This deviation from zero is interpreted as additional dissipation at particle surfaces and is denoted by ε^{*}_{pp}. Therefore, the use of a particle acceleration model for fluid-solid interactions in the PP-DNS approach leads to a different form of the mixture energy equation, that is

$$\frac{de^{(m)}}{dt}=-\varepsilon^{*}_{pp}-\varepsilon^{(f)}_{pp}, \tag{2.7}$$

which is now governed by the under-resolved viscous dissipation $\varepsilon^{(f)}_{pp}$ and the model for additional dissipation at particle surfaces ε^{*}_{pp}. We use our simulation data to assess the accuracy of the PP-DNS approach in predicting the evolution of $k^{(f)}$ and $k^{(p)}$, and also the true viscous dissipation $\varepsilon^{(f)}$ by quantifying ε^{*}_{pp} and $\varepsilon^{(f)}_{pp}$.

3. Numerical method

In the following sub-sections, we first introduce our PR-DNS approach followed by the PP-DNS methodology.

3.1. *Particle-resolved direct numerical simulation methodology*

For the PR-DNS approach, we use the particle-resolved uncontaminated fluid reconcilable immersed boundary method (PUReIBM) that has been described in detail by Tenneti *et al.* (2010). In PUReIBM, particles are represented in a Lagrangian frame of reference at time t by $\{\mathbf{X}^{(i)}(t),\ \mathbf{V}^{(i)}(t)\ i = 1...N_p\}$ where $\mathbf{X}^{(i)}(t)$ and $\mathbf{V}^{(i)}(t)$ are the position and velocity of the i^{th} particle, respectively, and N_p is the total number of particles. The position and translational velocity of the i^{th} particle evolve according to Newton's second law as

$$\frac{d\mathbf{X}^{(i)}(t)}{dt} = \mathbf{V}^{(i)}(t), \tag{3.1}$$

$$m^{(i)}\frac{\mathbf{V}^{(i)}(t)}{dt} = \mathbf{B} + \mathbf{F}_h^{(i)}(t) + \sum_{\substack{j=1 \\ j\neq i}}^{N_p} \mathbf{F}_{ij}^{(c)}(t), \tag{3.2}$$

where $\mathbf{B}$ is any external body force, $\mathbf{F}_h^{(i)}$ is the hydrodynamic force arising from the stress tensor at the particle surface, and $\mathbf{F}_{ij}^{(c)}$ is the contact force on the i^{th} particle as a result of collision with j^{th} particle. Particle-particle interactions are treated by using a soft-sphere model originally proposed by Cundall & Strack (1979). In the soft-sphere approach, the contact mechanics between two overlapping particles is modeled by a system of springs and dashpots in both normal and tangential directions. The particles considered in this study are assumed to be frictionless and elastic. Thus, the tangential component of the contact force as well as the normal dashpot damping coefficient are zero. Therefore, only the normal component of the contact force $\mathbf{F}_{\mathbf{n}ij}$ is considered at time t, and it is given by

$$\mathbf{F}_{n_{ij}} = k_n \delta_{ij} \hat{\mathbf{r}}_{ij}, \tag{3.3}$$

where k_n is the spring stiffness in the normal directions and $\hat{\mathbf{r}}_{ij}$ is the unit vector along the line of contact pointing from particle i to particle j. In the above expression, $\delta_{ij} = d_p - \mid \mathbf{X}^{(i)} - \mathbf{X}^{(j)} \mid$ is the overlap of a colliding pair of particles. The hydrodynamic and contact forces computed at each time step are used to evolve the position and translational velocity of particles by Eqs. (3.1) and (3.2), respectively.

In the fluid phase, the mass and momentum conservation equations solved by PUReIBM are

$$\nabla \cdot \mathbf{u} = 0, \tag{3.4}$$

and

$$\rho^{(f)}\frac{\partial \mathbf{u}}{\partial t} + \rho^{(f)}\mathbf{S} = -\mathbf{g}_{\mathrm{IBM}} + \mu^{(f)}\nabla^2\mathbf{u} + \mathbf{f}, \tag{3.5}$$

where $\mathbf{u}$ is the instantaneous velocity, $\mathbf{S} = \boldsymbol{\nabla}\cdot(\mathbf{uu})$ is the convective term in conservative form, $\mathbf{g}_{\mathrm{IBM}} = \boldsymbol{\nabla} p$ is the pressure gradient, $\mathbf{f}$ is the immersed boundary (IB) forcing that accounts for the presence of particles by ensuring the no-slip and no-penetration boundary conditions at the particle-fluid interface. The IB forcing in PUReIBM is non-zero only inside the solid particle. Thus, the equations in the fluid phase are not contaminated by the IB forcing. In our homogeneous and isotropic turbulence particle-laden flow setup, the governing equations for the fluctuating velocity and pressure variables are solved using a tri-periodic pseudo-spectral method, with the Crank-Nicolson scheme for the viscous terms, and an Adams-Bashforth scheme for the convective terms. A fractional

time-stepping method that is based on Kim and Moin's approach (Kim & Moin 1985) is used to advance the fluctuating velocity fields in time.

3.2. *Point-particle direct numerical simulation methodology*

For a dilute suspension ($\phi < 0.001$) with $d_p \leq \eta$, particles may be modeled as point sources of momentum and energy with respect to the fluid phase, and volume displacement effects in the fluid continuity and momentum equations can be neglected (Sundaram & Collins 1996). Fluid-particle coupling then amounts to determination of the appropriate drag law and numerical implementation of that drag law. When the particle Reynolds number is of order unity or less, the Stokes drag is assumed to be the leading order contribution in the drag law. We adopt this assumption in the current work.

In the point-particle DNS algorithm, particle motions are governed by the same dynamic Eqs. (3.1) and 3.2. However, the hydrodynamic force is now estimated using a drag law. In addition, the collisional force is assumed to be negligible. The fluid-phase mass and momentum equations are, respectively, the same as Eqs. (3.4) and (3.5) with the term $\mathbf{f}$ being replaced by $-\sum_{i=1}^{N_p} \mathbf{F}_h^{(i)} \delta(\mathbf{x} - \mathbf{x}_p)/V$ which represents the transfer of momentum between the fluid phase and solid particles. The fluid equations are solved using a second order method on a staggered mesh. Fluid and particles equations are advanced in time using a fourth order Runge-Kutta scheme. To calculate the Stokes drag force, fluid velocities at cell faces are interpolated to particle locations. Once the Stokes drag has been calculated by forming the relative velocity between the i^{th} particle and the interpolated fluid velocity, the force is projected back to the Eulerian grid using the same interpolation weights.

4. Results

We are interested in simulating a test case with $d_p = \eta$, where the PP-DNS approach holds, and that is also computationally feasible for the PR-DNS approach. Note that the computational resolution requirement for the PR-DNS approach increases inversely with the d_p/η ratio (Xu & Subramaniam 2010). The range of the particle Stokes number, Reynolds number and particle diameter considered in this study are, respectively, $\mathrm{St}_\eta = \mathcal{O}(1)$, $\mathrm{Re}_p = \mathcal{O}(1)$, and $d_p < \eta$, which represent regimes of interest for particle-based solar-power collectors. Although we match the non-dimensional parameters ($\mathrm{St}_\eta = 1$ and $\mathrm{Re}_p = 1$), we are now simulating larger particles that are less dense. This has consequences for the applicability of the steady drag model in the PP-DNS.

In the PR-DNS approach, the grid resolution across a particle should be sufficiently fine for the hydrodynamic boundary layer and velocity gradients at the particle surface to be accurately captured. In our problem, the grid resolution across each particle is $D_m = d_p/\Delta x = 12$. The large scales of isotropic turbulence are determined by the size of the computational box. In this study we considered two box sizes for our PR-DNS; A medium size box with a grid resolution 576^3 and large size box with a grid resolution 1152^3 that are, respectively, associated with turbulent Reynolds number $\mathrm{Re}_\lambda = 12$ and 27 based on the Taylor microscale length scale. Table 1 summarizes the physical and numerical parameters of the cases considered in this study. We choose the solid-phase volume fraction as $\phi = 0.001$ for solid particles that are uniformly distributed and initially at rest. We initialized the fluid-phase isotropic turbulence using the method of Rogallo (1981) with the energy spectrum function given by Pope (2000). Figure 1 shows a snapshot of the turbulent gas-solid flow in the large box.

TABLE 1. Physical and numerical parameters of the turbulent gas-solid flow simulations. The grid resolution requirement across a particle is applicable only to the PR-DNS approach.

Re_λ	ϕ	$\rho^{(p)}/\rho^{(f)}$	d_p/η	St	$\mathcal{L}/d_p$	D_m	N_p
12	0.001	18	1	1	48	12	210
27	0.001	18	1	1	96	12	1690

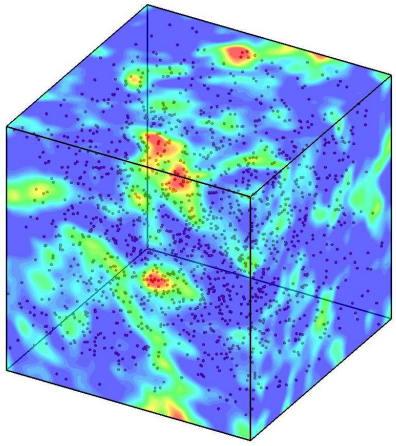

FIGURE 1. A snapshot of the large size turbulent gas-solid flow. The contour colors represent the intensity of the isotropic turbulence.

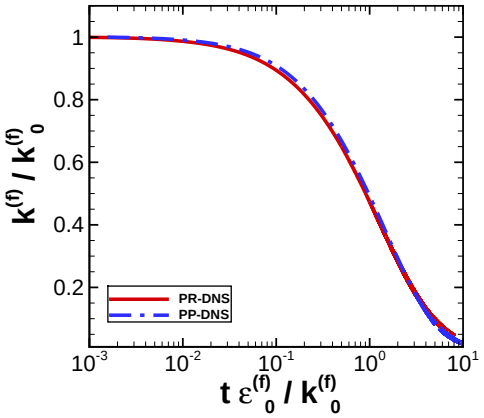

FIGURE 2. Comparison of the evolution $k^{(f)}$ between the PR-DNS and the PP-DNS approach.

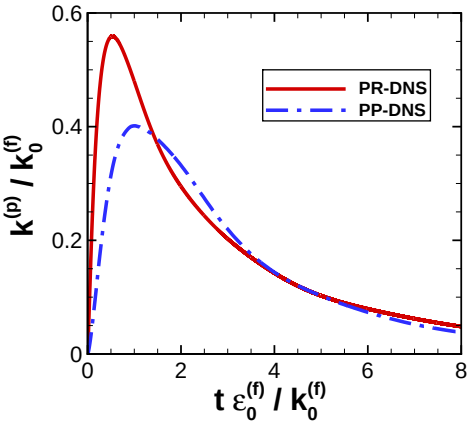

FIGURE 3. Comparison of the evolution $k^{(p)}$ between the PR-DNS and the PP-DNS approach.

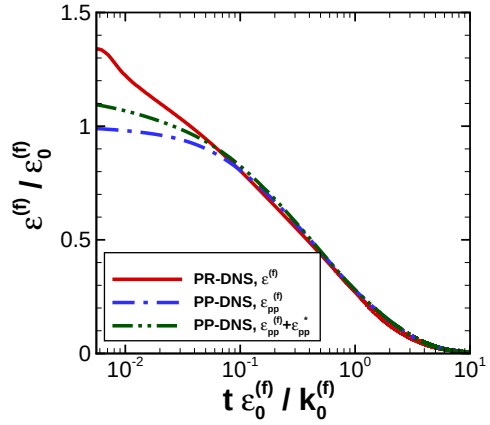

FIGURE 4. Comparison of the evolution of viscous dissipation between the PR-DNS and the PP-DNS approach.

Owing to the similarity of the results between $\mathrm{Re}_\lambda = 12$ and $\mathrm{Re}_\lambda = 27$ simulations, we present only the results for the case $\mathrm{Re}_\lambda = 12$. Figure 2 shows a comparison of the

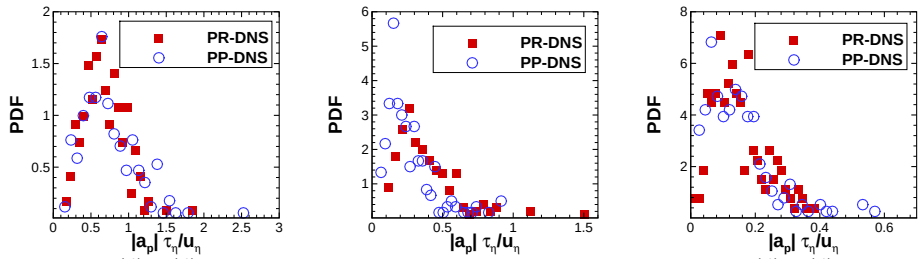

(a) $t\varepsilon_0^{(f)}/k_0^{(f)} = 0.2$ (b) At the peak of $k^{(p)}$ (c) $t\varepsilon_0^{(f)}/k_0^{(f)} = 3.0$

FIGURE 5. Comparison of particle acceleration PDFs between the PR-DNS and PP-DNS at three different instances.

evolution of kinetic energy in the gas-phase velocity fluctuations obtained from PR-DNS and PP-DNS. The PP-DNS result shows the same trend with a maximum difference of 3%. Note that the $k^{(f)}$ from PP-DNS is slightly overpredicted for $t\varepsilon_0^{(f)}/k_0^{(f)} < 3$ compared with that of PR-DNS. The evolution of solid-phase velocity fluctuations in Figure 3 indicates that the maximum value of $k^{(p)}$ in PP-DNS is about 30% less than the maximum value in PR-DNS. In addition, the maximum value in the PR-DNS occurs at $t\varepsilon_0^{(f)}/k_0^{(f)} = 0.5$, while it happens at $t\varepsilon_0^{(f)}/k_0^{(f)} = 1.0$ in the PP-DNS.

Quantification of viscous dissipation shown in Figure 4 indicates an increase of about 30% in the PR-DNS, when compared with the initial viscous dissipation $\varepsilon_0^{(f)}$ at the beginning of the simulation. Dissipation increases because particles that are initially at rest induce locally large strain rates in the hydrodynamic boundary layers around each particle. The viscous dissipation from the PP-DNS approach $\varepsilon_{pp}^{(f)}$, however, does not show any increase from the dissipation in single-phase decaying isotropic turbulence (not shown here). If we also account for the additional viscous dissipation in Eq. (2.6) that arises from using a particle acceleration model in PP-DNS (Sundaram & Collins 1996), only about one third of the additional dissipation at particle surface is recovered when compared with that of PR-DNS. After early stages of the simulations, particles relax to the local velocity of the flow field. Therefore, the strain rate at particle surfaces decreases and this leads to attenuation of viscous dissipation. Note that at $t\varepsilon_0^{(f)}/k_0^{(f)} = 0.1$ there is no significant difference in viscous dissipation between PR-DNS and PP-DNS, although PR-DNS shows slightly lower dissipation. Higher value of $k^{(p)}$ and $\varepsilon^{(f)}$ in PR-DNS indicates that the mechanism of momentum and energy transfer between the fluid-phase and the solid-phase is different between the two simulation approaches.

5. Discussion

In this section, we first assess the ability of PP-DNS to predict the true particle acceleration, and then examine the mechanism of energy transfer between the fluid phase and the solid phase.

5.1. *Particle acceleration PDF*

We extract the magnitude of the hydrodynamic acceleration experienced by each particle and construct the corresponding probability density functions (PDF). Note that statistical error due to a relatively low particle sample number yields relatively large confidence bounds on the data. The PDFs from the PR-DNS and the PP-DNS are compared at

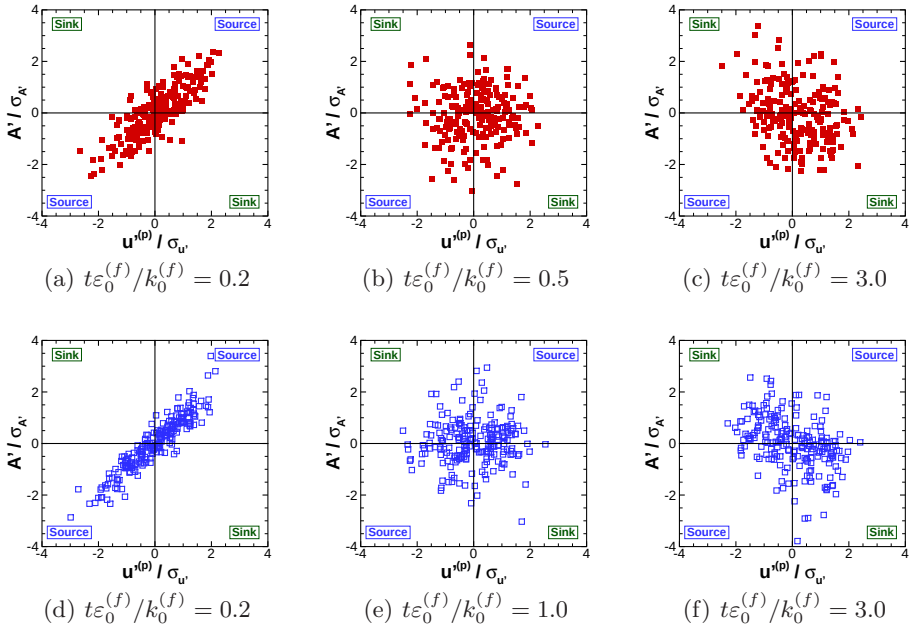

(a) $t\varepsilon_0^{(f)}/k_0^{(f)} = 0.2$ (b) $t\varepsilon_0^{(f)}/k_0^{(f)} = 0.5$ (c) $t\varepsilon_0^{(f)}/k_0^{(f)} = 3.0$

(d) $t\varepsilon_0^{(f)}/k_0^{(f)} = 0.2$ (e) $t\varepsilon_0^{(f)}/k_0^{(f)} = 1.0$ (f) $t\varepsilon_0^{(f)}/k_0^{(f)} = 3.0$

FIGURE 6. Scatter plot of $\mathbf{u}'^{(p)}$-$\mathbf{A}'$ that corresponds to the quantification of the source and the sink of solid-phase kinetic energy. The first row of figures with filled symbols corresponds to PR-DNS, and the second row of figures with hollow symbols belongs to PP-DNS. The first and last columns are extracted at a time when $k^{(p)}$ is increasing and decreasing, respectively, while the middle column is extracted at the time when $k^{(p)}$ reaches the maximum value. In these plots, the horizontal axes are normalized by the standard deviation of particle velocity fluctuations, and the vertical axes are normalized by the standard deviation of particle accelerations. The values of $\sigma_{\mathbf{u}'}$ and $\sigma_{\mathbf{A}'}$ are given in Table 2.

three times corresponding to increasing, maximum, and decreasing $k^{(p)}$, shown in Figure 5(a-c), respectively. The variance of PP-DNS and PR-DNS accelerations decreases in time as the particles equilibriate with the local fluid velocity. The PDFs are qualitatively similar between the PR-DNS and PP-DNS cases, although the PDF tails, corresponding to the maximum particle acceleration, do not match well at any of the times. In addition, as observed in Figure 5(b), the peak values of the PDFs in the PR-DNS and the PP-DNS as well as the corresponding accelerations where these peaks occur are different.

The deviation of PP-DNS particle accelerations from the PR-DNS true accelerations suggests that other types of hydrodynamic forces such as the virtual mass force, the history force, and the lift forces, may also be important and should be considered in LE simulation of a gas-solid flows (Crowe *et al.* 2011).

5.2. *Interphase TKE trasnfer*

Recall from Eq. (2.2) that the rate of change of solid-phase kinetic energy is governed by the interphase TKE transfer term. The interphase TKE transfer has the form

$$\Pi^{(p)} = \left\langle \mathbf{u}'^{(p)} \cdot \mathbf{A}' \right\rangle, \tag{5.1}$$

which is the particle velocity-acceleration covariance. Tenneti *et al.* (2010) showed that the interphase TKE transfer acts as either a source or a sink of $k^{(p)}$ and can be quantified by a quadrant analysis. Figure 6(a) shows the fluctuating velocity-acceleration scatter

TABLE 2. Standard variation of particle velocity fluctuation and particle acceleration in the PR-DNS and the PP-DNS at three different times in accordance with Figure 6. These quantities are normalized by the initial Kolmogorov velocity scale u_η and time scale τ_η.

$t\varepsilon_0^{(f)}/k_0^{(f)}$	0.2		At the peak of $k^{(p)}$		3.0	
	$\sigma_{\mathbf{u}'}/u_\eta$	$\sigma_{\mathbf{A}'}\tau_\eta/u_\eta$	$\sigma_{\mathbf{u}'}/u_\eta$	$\sigma_{\mathbf{A}'}\tau_\eta/u_\eta$	$\sigma_{\mathbf{u}'}/u_\eta$	$\sigma_{\mathbf{A}'}\tau_\eta/u_\eta$
PR-DNS	1.13	0.41	1.31	0.25	0.79	0.10
PP-DNS	0.63	0.47	1.11	0.18	0.80	0.10

plot of PR-DNS at $t\varepsilon_0^{(f)}/k_0^{(f)} = 0.2$. Those points that lie in quadrants 1 and 3 contribute to the source of $k^{(p)}$ whereas those in quadrants 2 and 4 contribute to the sink.

Figure 6 compares scatter plots of $\mathbf{u}'^{(p)}$-$\mathbf{A}'$ between the PR-DNS and PP-DNS during the increase, at maximum, and during the decrease of $k^{(p)}$. Figure 6(a,d) shows that in the region where $k^{(p)}$ increases, the contribution to the source is much more than the contribution to the sink. Therefore, the correlation on the right-hand side of Eq. (5.1) is positive that leads to the increase of $k^{(p)}$. When $k^{(p)}$ is at maximum, the scatter points are approximately uniformly distributed in all quadrants as shown in Figure 6(b,e), suggesting that the correlation is approximately zero. During the decay of $k^{(p)}$, the contribution to the sink is slightly more than the contribution to the source as shown in Figure 6(c,f), which leads to the attenuation of $k^{(p)}$. Although these normalized plots in each column comparing the PR-DNS with PP-DNS results are similar, the standard variations of $\sigma_{\mathbf{u}'}$ and $\sigma_{\mathbf{A}'}$ between the PR-DNS and PP-DNS are quite different at the first two time instances as shown in Table 2. These differences substantially change the mechanism of energy transfer from one phase to another which leads to a difference in the evolution of $k^{(p)}$ between the PR-DNS and PP-DNS.

Because particle acceleration plays a key role in the interphase transfer of energy to and from the solid phase, any inaccuracy in the prediction of particle acceleration affects the evolution of $k^{(p)}$ as well as the $k^{(f)}$ in the neighborhood of each particle. These effects are non-linear and feedback on each other. Therefore, accurate modeling of the particle acceleration term is crucial for accurate determination of both particle and fluid statistics.

6. Conclusion

In this study, we performed PR-DNS and PP-DNS of a turbulent particle-laden suspension in a regime identified by $\mathrm{St}_\eta = 1$, $\mathrm{Re}_p = 1$ and $d_p/\eta = 1$. Comparison of decaying isotropic turbulence shows similar trends for the fluid-phase kinetic energy between the PR-DNS and PP-DNS cases. However, $k^{(p)}$ is significantly different in terms of the maximum value and the time at which the maximum value occurs. This deviation is associated with the difference in the transfer of energy between the fluid phase and the solid phase in the two approaches. The covariance of particle acceleration-particle velocity acts as the source and sink of the solid-phase kinetic energy. Use of the Stokes drag law in the PP-DNS approach leads to inaccuracy in prediction of particle acceleration that in turn affects the solid-phase kinetic energy. The Stokes drag cannot solely represent the gas-solid interaction. Other contributions such as the virtual mass force

or history force are also important at low $\rho^{(p)}/\rho^{(f)}$. This study will open the door for more simulations to be performed that directly compare PR-DNS and PP-DNS where the aforementioned hydrodynamic forces are also accounted for. As a validation tool, particle-resolved simulations will enable testing of theory established by point-particle simulations. Comparison of PR-DNS and PP-DNS will shed light on flow physics and lead to improvement of point-particle acceleration models.

Acknowledgements

We acknowledge the National Science Foundation (NSF) for partial support from award CBET 1134500 and NSF Graduate Research Fellowship under Grant No. DGE-114747. We also acknowledge the NSF for the awards CBET 0960306 and CNS 1229081 for providing computing resources that have contributed to the research results reported within this report. Any opinion, findings, and conclusions or recommendations expressed in this material are those of the authors and do not necessarily reflect views of the National Science Foundation.

REFERENCES

Balachandar, S. & Eaton, J. K. 2010 Turbulent dispersed multiphase flow. *Annu. Rev. Fluid Mech.* **42**, 111–133.

Crowe, C., Schwarzkopf, J., Sommerfeld, M. & Tsuji, Y. 2011 *Multiphase Flows with Droplets and Particles*. CRC Press.

Cundall, P. A. & Strack, O. D. L. 1979 A discrete numerical model for granular assemblies. *Geotechnique* **29**, 47–65.

Kim, J. & Moin, P. 1985 Application of a fractional-step method to incompressible Navier-Stokes equations. *J. Comput. Phys.* **59**, 308–323.

Pai, M. G. & Subramaniam, S. 2009 A comprehensive probability density function formalism for multiphase flows. *J. Fluid Mech.* **628**, 181–228.

Pope, S. B. 2000 *Turbulent Flows*. Port Chester, NY: Cambridge University Press.

Rogallo, R. S. 1981 *Numerical experiments in homogeneous turbulence.* NASA Technical Report no. 81835.

Sundaram, S. & Collins, L. R. 1996 Numerical considerations in simulating a turbulent suspension of finite–volume particles. *J. Comput. Phys.* **124**, 337–350.

Tenneti, S., Garg, R., Hrenya, C., Fox, R. & Subramaniam, S. 2010 Direct numerical simulation of gas-solid suspensions at moderate Reynolds number: Quantifying the coupling between hydrodynamic forces and particle velocity fluctuations. *Powder Tech.* **203** (1), 57–69.

Xu, Y. & Subramaniam, S. 2007 Consistent modeling of interphase turbulent kinetic energy transfer in particle-laden turbulent flows. *Phys. Fluids* **19** (8), 085101.

Xu, Y. & Subramaniam, S. 2010 Effect of particle clusters on carrier flow turbulence: A direct numerical simulation study. *Flow Turbul. Combust.* **85**, 735–761.

Zamansky, R., Coletti, F., Massot, M. & Mani, A. 2014 Radiation induces turbulence in particle-laden fluids. *Phys. Fluids* **26** (7).